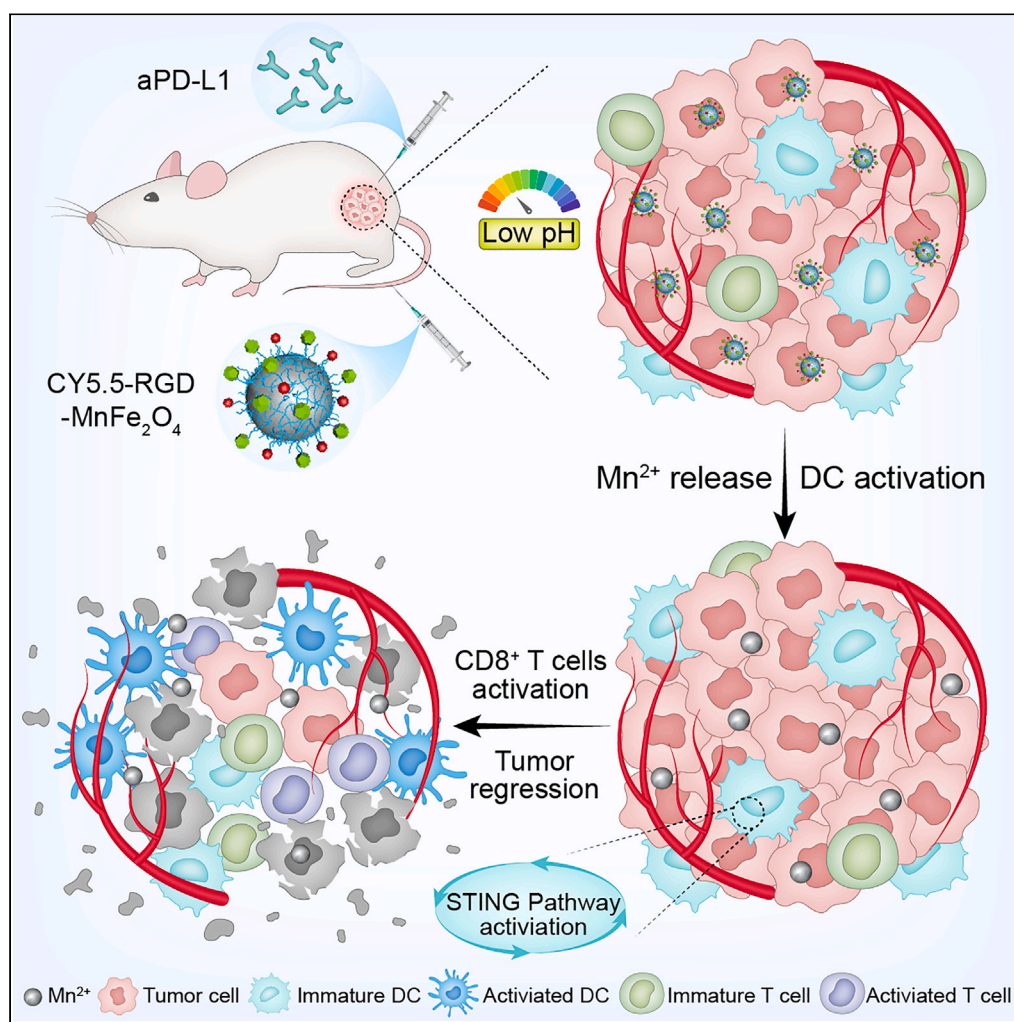**Article**

RGD targeted magnetic ferrite nanoparticles enhance antitumor immunotherapeutic efficacy by activating STING signaling pathway

Guangyuan Shi,
Xiaoli Liu, Yang Du,
Jie Tian

liuxiaoli0108@xjtu.edu.cn (X.L.)
yang.du@ia.ac.cn (Y.D.)
jie.tian@ia.ac.cn (J.T.)

Highlights
We designed manganese ferrite nanoparticles with RGD modification (RGD-MnFe₂O₄)

They activate the STING signaling pathway to improve tumor immunotherapy

RGD-MnFe₂O₄ nanoparticles exhibited specific tumor-targeted binding

RGD-MnFe₂O₄ nanoparticles enhanced the antitumor effect of aPD-L1 blockade

Article

RGD targeted magnetic ferrite nanoparticles enhance antitumor immunotherapeutic efficacy by activating STING signaling pathway

Guangyuan Shi,[1,2] Xiaoli Liu,[3,*] Yang Du,[2,4,*] and Jie Tian[5,6,*]

SUMMARY

Manganese has been used in tumor imaging for their ability to provide T1-weighted MRI signal. Recent research find Mn^{2+} can induce activation of the stimulator of interferon gene (STING) pathway to create an active and favorable tumor immune microenvironment. However, the direct injection of Mn^{2+} often results in toxicity. In this study, we developed an RGD targeted magnetic ferrite nanoparticle (RGD-$MnFe_2O_4$) to facilitate tumor targeted imaging and improve tumor immunotherapy. Magnetic resonance imaging and fluorescence molecular imaging were performed to monitor its *in vivo* biodistribution. We found that RGD-$MnFe_2O_4$ showed active tumor targeting and longer accumulation at tumor sites. Moreover, RGD-$MnFe_2O_4$ can activate STING pathway with low toxicity to enhance the PD-L1 expression. Furthermore, combining RGD-$MnFe_2O_4$ and anti-PD-L1 antibody (aPD-L1) can treat several types of immunogenic tumors through promoting the accumulation of tumor-infiltrating cytotoxic T cells. In general, our study provides a promising new strategy for the targeted and multifunctional theranostic nanoparticle for the improvement of tumor immunotherapy.

INTRODUCTION

Immune checkpoint blockade (ICB), including anti-PD-1, anti-PD-L1, and anti-CTLA-4 antibodies, has become one of the most successful cancer therapies.[1–6] However, most cancer patients remain unresponsive to ICB therapies, mainly because most tumors are immunologically "cold".[7–9] Hence, optimizing the tumor immune microenvironment may improve the immunotherapeutic efficacy.[10] For example, some trials that attempted to create a "hot" tumor immune microenvironment have shown exciting therapeutic results in patients, such as using hypoxia inhibitors or radiotherapy to improve the response rate.[9,11] Antigen recognition and cross-presentation by antigen-presenting cells (APCs), such as dendritic cells (DCs) and macrophages, are key processes for the activation of cytotoxic T cells.[12] Recent studies have shown that the stimulator of interferon gene (STING) signaling facilitated macrophage polarization into the pro-inflammatory subtype and DC activation by stimulating CD80 and CD86 expression.[13] In addition, activation of the STING pathway in cancer cells enhances PD-L1 expression, indicating that cancer cells may be more sensitive to ICB therapy.[14] X. An et al., 2019 found that patients with high STING protein expression showed a clinical benefit from anti-CTLA-4 therapy and had longer survival time. High expression of cyclic guanosine triphosphate-adenosine triphosphate synthase (cGAS) or STING was positively correlated with the infiltration of immune cells in pan-cancer.[15] Several studies have shown that the combined administration of STING activators and ICB antibodies shows better therapeutic effects than ICB alone.[7,16,17]

The innate immune regulatory function of the STING pathway was discovered in 2008.[18] As the study of the STING pathway has progressed, an increasing amount of evidence has shown that the STING signaling is important in the activation of adaptive immunity in cancer.[7,19,20] Generally, free DNA in the cytoplasm is considered harmful because it may be involved in pathogen infection, cellular senescence, and many other abnormal events. Once cGAS binds to double-stranded DNA, it is activated and cyclic guanosine triphosphate-adenosine triphosphate (cGAMP) will be synthesized by adenosine 5′-triphosphate and guanosine 5′-triphosphate. cGAMP then activates STING and promotes the phosphorylation of TBK1 and IRF3, leading to the production of a wide range of immunostimulatory molecules like CD86 and MHC-II.[21–23] Followed by increased costimulatory signals necessary for T cell activation and the induction of immunogenic cell death of tumor cells and inhibition of tumor growth.[24]

Direct activation of STING by agonists through intratumoral or intravenous injections resulted in effective antitumor therapy in a subcutaneous tumor model.[25–27] However, intratumoral injections are limited to superficial tumors and have poor repeatability. Agonists do not

[1]University of Science and Technology of China, Hefei 230026, China
[2]CAS Key Laboratory of Molecular Imaging, Beijing Key Laboratory of Molecular Imaging, Institute of Automation, Chinese Academy of Sciences, Beijing 100190, China
[3]Northwest University, Xi'an 710127, China
[4]University of Chinese Academy of Sciences, Beijing 100080, China
[5]Science and Engineering, Beihang University, Beijing 100191, China
[6]Lead contact
*Correspondence: liuxiaoli0108@xjtu.edu.cn (X.L.), yang.du@ia.ac.cn (Y.D.), jie.tian@ia.ac.cn (J.T.)
https://doi.org/10.1016/j.isci.2024.109062

specifically bind to tumors and are likely to be degraded *in vivo*. Hence, agonists should be used at high concentrations to ensure efficacy. However, excess agonists are likely to cause unnecessary and harmful side effects. An increasing number of nanomaterials have been developed to activate the STING pathway in cancer immunotherapy so that antitumor therapy can be activated more efficiently with less toxicity.[28–30] Phosphatidylserine, mesoporous silica nanoparticles, and many other materials have been used in immunotherapy associated with STING pathway activation, which enables efficient delivery of immunostimulants to intratumoral APCs.[17,31–33]

Recently, Liu et al. found that Mn^{2+} could activate innate immunity via the STING pathway in a lymphocytoma model, which is expected to reverse tumor immune microenvironment inhibition.[34] Activation of the STING pathway by $MnCl_2$ via intratumoral injection enhances the therapeutic efficacy of anti-PD-L1 antibodies.[17] Mn^{2+} is advantageous in tumor imaging and therapy because it enhances T1 weighted magnetic resonance imaging (MRI) signal and activates the STING signaling pathway.[35,36] However, intraperitoneal injection of 15 mg Mn^{2+}/kg induce neurotoxicity in rats, and intravenous injection (5–10 mg Mn/kg) affect cardiac function.[37,38] Hou et al. developed acid-triggered nanoparticles called nano-scaled amorphous porous manganese phosphate, which carried DNA-damage chemotherapy drugs to activate STING pathway more efficiently, and showed tumor-targeting capacity and excellent antitumor efficacy.[39] Hence, manganese-containing nanoparticles with the ability to generate Mn^{2+} in an acidic tumor microenvironment have attracted our attention.[39–43]

Hence, the aim of this study is to develop a tumor-targeting and multifunctional manganese-containing nanoparticle, Cy5.5-RGD-MnFe$_2$O$_4$ (Cy5.5-RGD-NP). We utilized c(RGDyK) as the targeting element, and it can specifically bind to αvβ3-integrin highly expressed in various tumors.[44–47] The biodistribution and tumor targeting effect of Cy5.5-RGD-NP was examined using fluorescence molecular imaging (FMI) and MRI. Moreover, the activation of STING signaling pathway to regulate the tumor immune microenvironment was investigated. Finally, this multifunctional magnetic ferrite nanoparticle was further utilized in combination with anti-PD-L1 antibody (aPD-L1) to improve immunotherapeutic efficacy. Our study may provide new immunomodulating strategy to improve the antitumor immunotherapeutic efficacy with less immunotoxicity (Scheme 1).

RESULTS

Characteristic of RGD-NPs

The design and synthesis procedure were shown in Figure 1A. Transmission electron microscopy (TEM) images showed that RGD-NP were monodispersed and spherical in morphology with a mean diameter of approximately 8 nm (Figure 1B). Zeta potential results further verified the excellent colloidal stability of these nanoparticles in various solutions (Figures 1C and S1). The hydrodynamic diameter of RGD-NP ranged from 10 nm to 12 nm in water and remained unchanged for 19 days (Figure 1D). RGD-NP showed similar hydrodynamic diameter in normal saline and cell-culture medium (DMEM), which verified the stability of RGD-NPs under physiological environment (Figure 1E). XPS results showed that iron is in the valence state of III and manganese is in the valence state of II based on The International XPS database (Figures S2A and S2B), which is in accord with the MnFe$_2$O$_4$ formula. The release kinetics of Mn^{2+} from the nanoparticles were measured through inductively coupled plasma-mass spectrometry (ICP-MS) (Figure S2C). The UV-Vis absorption spectrum and fluorescence spectrum were shown in Figures 1F and 1G, which indicated the imaging capability of Cy5.5-RGD-NP.

The *in vitro* fluorescence microscopic imaging data showed that there was stronger red fluorescence detected on the targeted binding of Cy5.5-RGD-NP to CT26-GFP tumor cells than control Cy5.5-NP, and more blue dots detected in the Cy5.5-RGD-NP treated cells compared to the Cy5.5-NP for the prussian blue staining (Figure 1H). The flow cytometry data also confirmed the previous observation (Figure 1I). These data suggested that RGD-NP can specifically bind to CT26 tumor cells *in vitro*.

Specific tumor-targeted binding of RGD-NP

Based on *in vitro* data, we further performed *in vivo* FMI and MRI dual-modality imaging experiments. CT26 tumor-bearing mice were intravenously injected with 0.1 mg of Cy5.5-NP or Cy5.5-RGD-NP. The FMI data indicated the increased accumulation of Cy5.5-RGD-NP at the tumor site over time, whereas Cy5.5-NP showed less accumulation in the tumor (Figure 2A). The signal to background ratio (SBR) in the Cy5.5-RGD-NP group was significantly higher than that of Cy5.5-NP group (Figure 2B). The *ex vivo* FMI data showed a higher tumor fluorescence signal in the Cy5.5-RGD-NP group than Cy5.5-NP group. Weak fluorescence was detected in the liver, suggesting that the nanoparticles were mainly metabolized through liver (Figure 2C). The T1-weighted MRI data showed an increased MRI signal in Cy5.5-RGD-NP treated tumors as early as 15 min post-injection compared to the Cy5.5-NP group (Figure 2D). We further quantify the level of Fe and Mn elements in the tumor and major organs at 6 h post-tail vein injection through ICP-MS (Figures S2D and S2E). The data showed higher distribution of Fe and Mn elements in the Cy5.5-RGD-NP treated tumors compared to the Cy5.5-NP. Based on the previous FMI and MRI data, our developed RGD-NPs were shown to have a more tumor-targeted binding and longer retention at tumor sites than the nanoparticles without RGD modification. The expression of intergrin on CT26 and tumor tissues were confirmed by immunohistochemical staining (Figure S3).

RGD-NPs activate STING signaling both *in vitro* and *in vivo*

It is reported that Mn^{2+} could activate STING signal in the THP-1 cell line.[34] In our study, western blot data showed that Mn^{2+} activated STING signaling in DC2.4 cells, an immortalized DC cell line, in a dose-dependent manner (Figure 3A). Activation of the STING pathway promotes the phosphorylation of TBK1, leading to the production of a wide range of immunostimulatory molecules. Thus, the *p*-TBK1 level is an important marker of STING pathway activation.[8–10] *p*-TBK1 was highly expressed in the Mn^{2+}-treated group, indicating that the STING pathway was activated. When we treated BMDCs with control nanoparticles or RGD-NPs, using cGAMP and Mn^{2+} as positive controls, both control
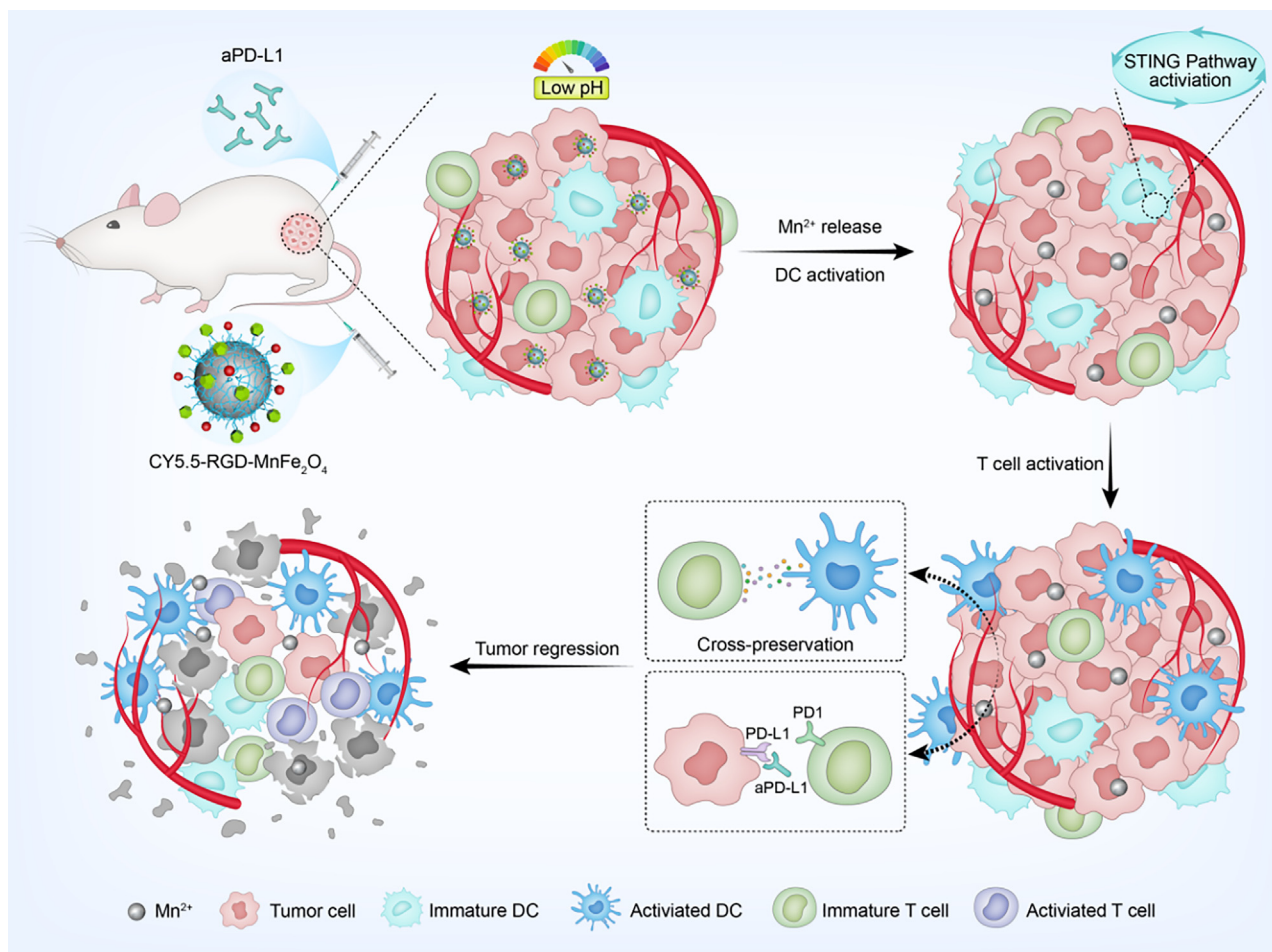
Scheme 1. Schematic illustration of RGD-MnFe₂O₄ nanoparticles for enhancing the immunotherapeutic efficacy of aPD-L1

nanoparticles and RGD-NPs activated the STING signal in BMDCs *in vitro*, with RGD-NPs inducing relatively higher *p*-TBK1 protein expression than the control nanoparticles (Figure 3B). Consistent with previous reports, we observed that STING protein translocated from the cytoplasm into the nucleus after RGD-NP treatment, indicating the activation of STING signaling (Figure 3C).[24]

Based on the *in vitro* data, we further treated CT26 subcutaneous tumors with control nanoparticles or RGD-NPs via intravenous injection to test whether RGD-NPs could activate the STING signal *in vivo*. The data showed that RGD-NPs increased *p*-TBK1 expression levels *in vivo*, which indicated activation of the STING pathway in the tumor 24 h post-injection of 0.1 mg of RGD-NP (Figure 3D). Moreover, PD-L1 protein expression was upregulated upon RGD-NP treatment, indicating its potential with combined aPD-L1 treatment. We also tested the expression levels of immune-related cytokines using real-time PCR. RGD-NP treatment decreased the expression level of immunosuppressive factors such as Arg and IL-10 and induced the expression of immunostimulatory cytokines such as IL-12 and IFN-β, which indicated the activation of antitumor immunity (Figure 3E). In general, we demonstrated that RGD-NPs could specifically and effectively activate the STING signaling pathway and upregulate PD-L1 expression in tumors.

RGD-NPs in combination with aPD-L1 enhance the antitumor efficacy

It is reported that activation of the STING pathway via subcutaneous injection of cGAMP can enhance the antitumor effect of PD-L1 blockade.[7] In our study, we also found that RGD-NP upregulated PD-L1 expression and activated the STING signaling pathway. Hence, we tested the immunotherapeutic effects of RGD-NPs in combination with aPD-L1 on different immunogenic tumors, such as B16F10, CT26, and 4T1 tumors. We found that both aPD-L1 and RGD-NP treatment delayed B16F10, CT26, and 4T1 tumor growth to a certain extent. We did not find that NP showed obvious antitumor effect (Figures S4A and S4B). However, in all therapeutic animal models, RGD-NP dramatically improved the antitumor effects of aPD-L1 compared to those of aPD-L1 or RGD-NP alone by decreasing tumor volume (Figures 4A–4C). No obvious body weight changes were observed among the groups, indicating that the combined RGD-NPs and aPD-L1 treatment did not exhibit obvious toxicity (Figures 4D–4F). After treatment, the CT26 tumors were dissected and weighed, and RGD-NP + aPD-L1 showed the most effective inhibition of tumor growth compared to other groups (Figures 4G and 4H).
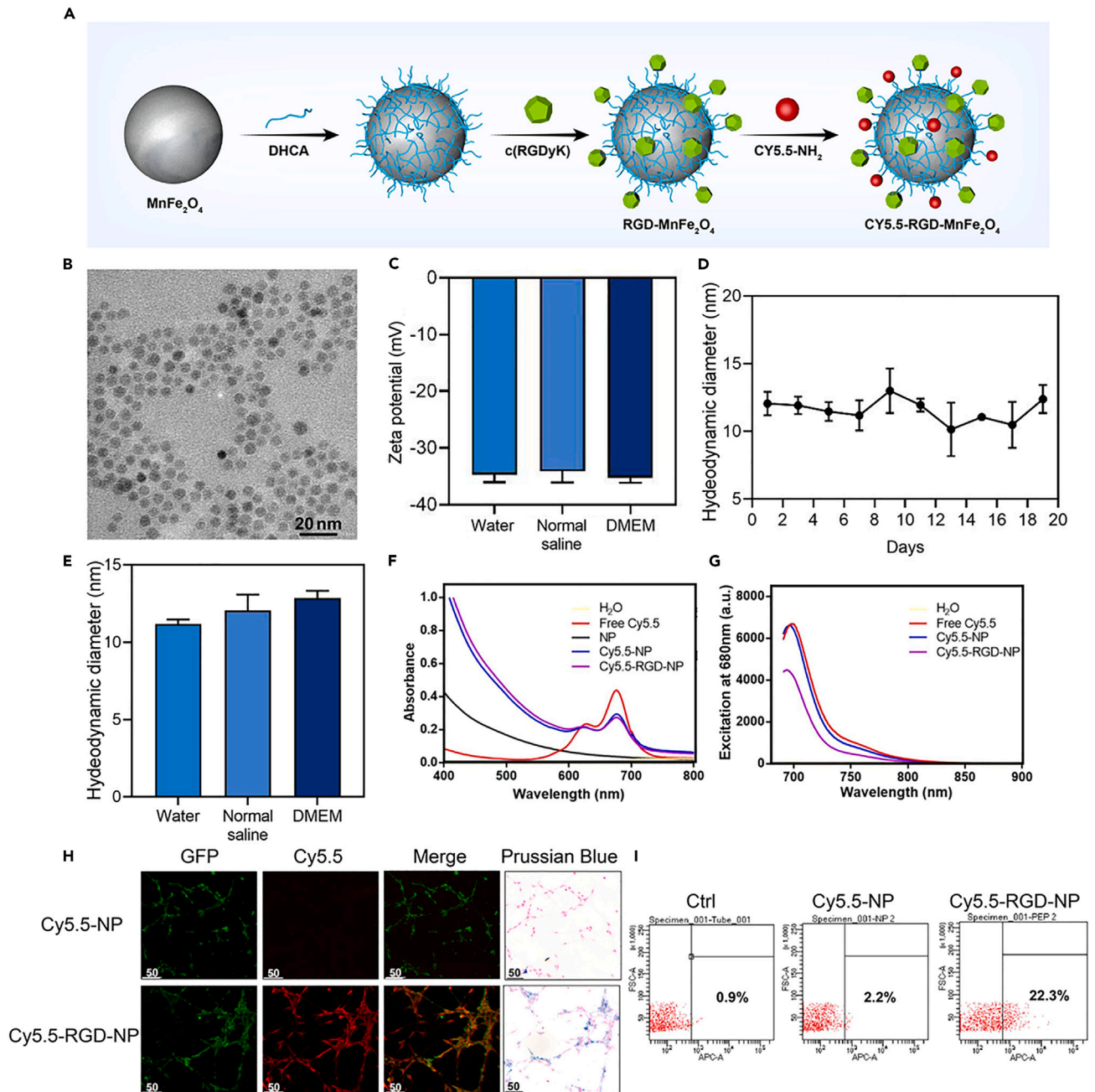
Figure 1. Preparation and characterization of RGD-NP

(A) Synthesis procedure of RGD-NP.

(B) TEM images of RGD-NP.

(C) Surface charges (zeta-potential) of RGD-NP in specific solution.

(D) Hydrodynamic diameter of RGD-NP in water during 19 days. Data are showed in mean $\pm$ SD.

(E) Hydrodynamic diameter of RGD-NP in different solution on the day 19th.

(F and G) Absorption spectrum and emission fluorescence spectrum of Cy5.5-RGD-NP and other control nanoparticles.

(H) Immunofluorescence imaging of CT26-GFP tumor cells treated with Cy5.5-RGD-NP and Cy5.5-NP, respectively Scale bar, 50 μm.

(I) Flow cytometry of CT26-GFP cells treated with different nanoparticles. Data are represented as mean $\pm$ SEM. (ns: $p > 0.05$, *: $p < 0.05$, **: $p < 0.01$, ***: $p < 0.001$, ****: $p < 0.001$).
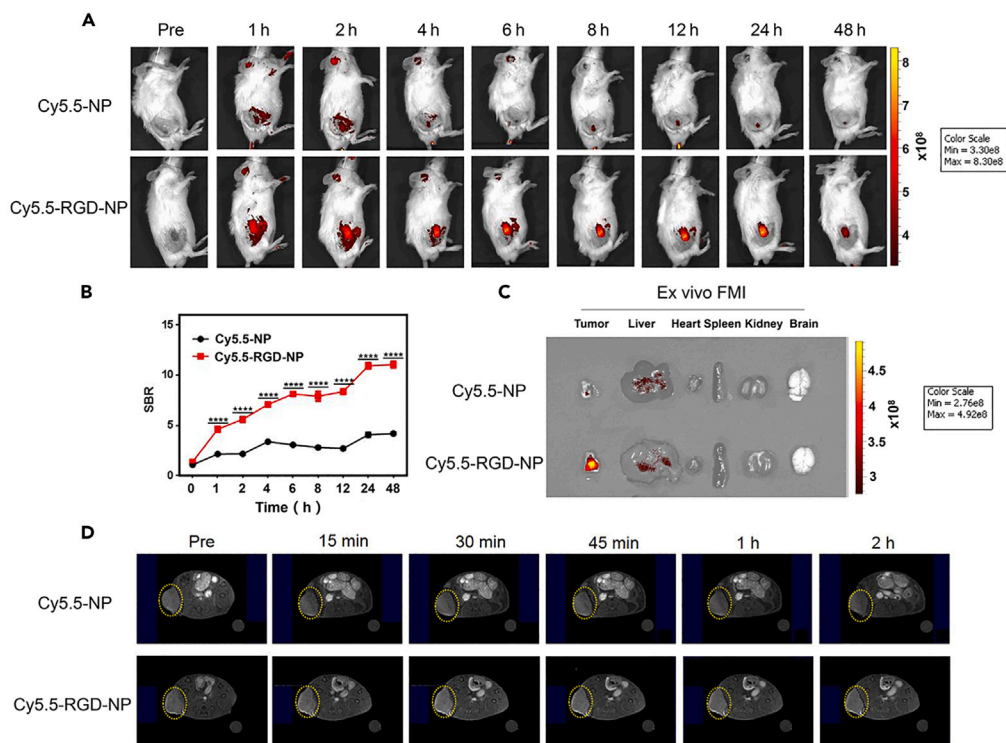
Figure 2. Specific tumor targeted FMI/MRI imaging of RGD-NPs in both *in vivo* and *ex vivo* CT26 tumor bearing mice

(A) FMI of CT26 tumor-bearing mice treated with Cy5.5-NP or Cy5.5-RGD-NP at different time points.

(B) The signal-to-background ratio (SBR) of *in vivo* FMI results.

(C) *Ex vivo* FMI of tumors and internal organs at 48 h post-injection of nanoparticles.

(D) The T1-weighted MRI of CT26 tumors at different time points. Data are represented as mean ± SEM. (ns: $p > 0.05$, *: $p < 0.05$, **: $p < 0.01$, ***: $p < 0.001$, ****: $p < 0.001$).

RGD-NP promote the infiltration of CTLs into tumors

To investigate how RGD-NPs enhance the antitumor effects of PD-L1 blockade via the STING pathway, flow cytometry was performed to analyze TILs during CT26 immunotherapy. Increased numbers of tumor-infiltrating CD4$^+$ and CD8$^+$ T cells are important indicators of immunotherapy.[48] PD-L1 blockade treatment increased CD8$^+$ and CD8$^+$CD69$^+$ T cell infiltration in tumors compared to PBS group (Figure 5A), and combined treatment with RGD-NPs and PD-L1 blockade further increased the number of CD8$^+$CD69$^+$ T cells (activated CD8$^+$ T cells) (Figure 5B). Increased CD86$^+$ DCs were also found in combined treatment group compared to the aPD-L1 group (Figure 5C). Neither RGD-NP treatment nor the PD-L1 blockade alone had a significant effect on CD4$^+$ T cells. However, the combined treatment increased the number of activated CD4$^+$ T cells compared to that in the RGD-NP group (Figures 5D and 5E). We then analyzed the protein samples of tumors and tumor-draining lymph nodes (TDLNs) using western blotting. We detected enhanced *p*-TBK1 protein expression levels in both tumors and TDLNs, indicating relatively high STING pathway activity in the combined treatment group compared to other treatment groups (Figures 5F and 5G). We found similar therapeutic results in 4T1 and B16F10 (Figures S5 and S6). We also performed immunohistochemistry to confirm the increased CD8$^+$ T cell levels after combined RGD-NP + aPD-L1 treatment and macrophages polarized from CD206$^+$ M2 macrophages into CD86$^+$ M1 macrophages (Figures 5H and S7). Overall, RGD-NPs could create a better immune microenvironment for PD-L1 blockade therapy, followed by a stronger immune response to the tumor and a more efficient reduction in tumor burden. The CCK8 assay showed that RGD-NP were relatively safe at different doses for 48 h (Figure S8A). We did not observe hepatic dysfunction based on aspartate transaminase (AST)/alanine transaminase (ALT) results or abnormalities in internal organs such as the heart, liver, spleen, brain, and kidney through H&E staining (Figures S8B–S8D), thereby excluding the toxic effects of RGD-NPs *in vivo*.

DISCUSSION

In our study, we designed a new tumor-targeting manganese ferrite theranostic nanoparticle RGD-MnFe$_2$O$_4$. FMI/MRI data showed increased accumulation and longer retention of RGD-NPs in CT26 tumors than nanoparticles without RGD peptide. The manganese activated the STING pathway, which further enhanced the antitumor effect of PD-L1 blockade with no obvious toxicity. The activated CD8$^+$ T cells and activated DCs were significantly increased in tumors in the combined aPD-L1 treatment group compared to the aPD-L1 and RGD-NP treatment alone groups. Our study shows that RGD-MnFe$_2$O$_4$ can function as an efficient therapeutic platform for
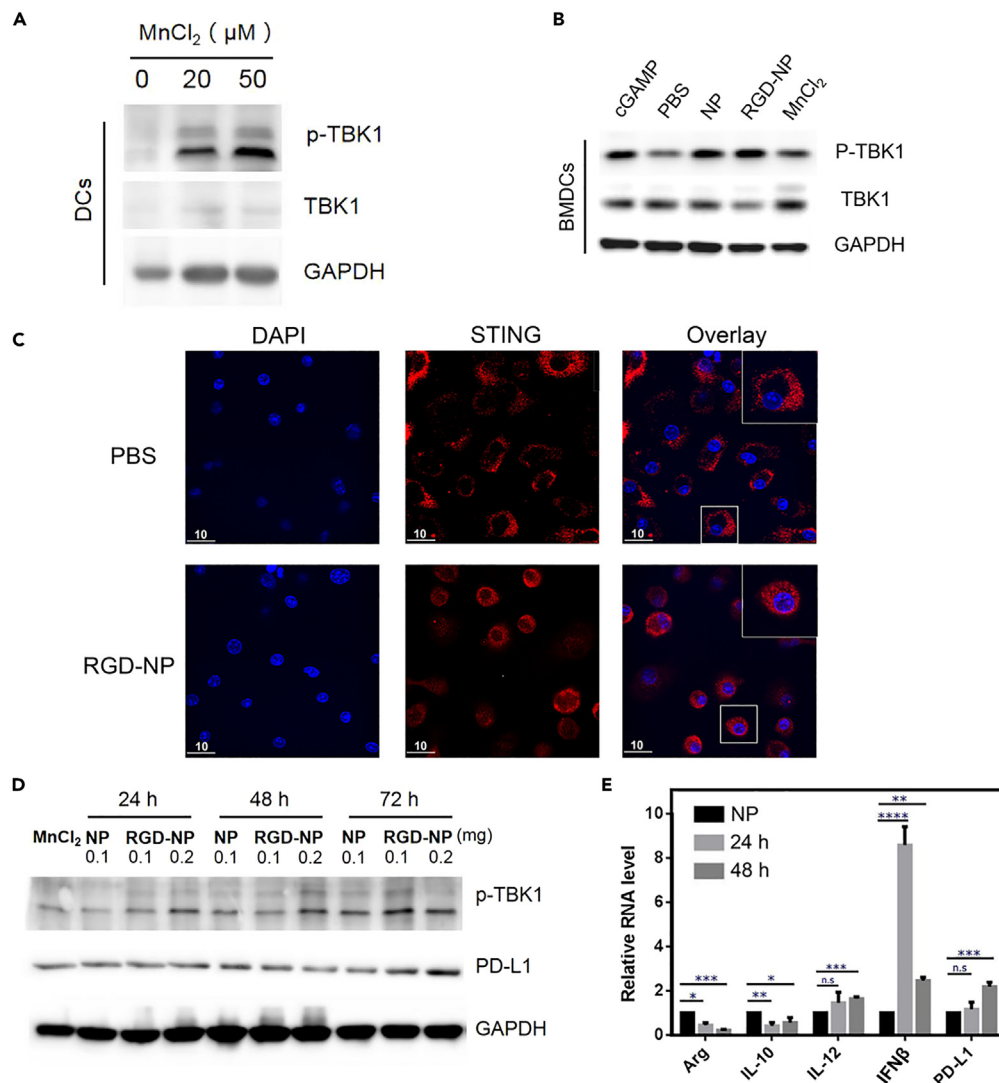
Figure 3. RGD-NPs activate STING signaling *in vitro*

(A) Western blot (WB) analysis of STING activation in DC2.4 cells treated with different concentrations of $MnCl_2$.

(B) WB analysis of STING activation in BMDCs treated with nanoparticles (NP) and RGD-NPs. cGAMP and $MnCl_2$ were utilized as positive controls.

(C) Immunofluorescence staining of STING (red) and nucleus (blue) in BMDCs treated with NP and RGD-NP. Scale bar, 10 μm.

(D) Western blot analysis of *p*-TBK1 and PD-L1 expression in tumors treated with 0.1 mg NP or different concentrations of RGD-NP for 24, 48, or 72 h.

(E) Real-time PCR analysis of immuno-related cytokine expression treated with RGD-NP. Data are represented as mean ± SEM. (ns: $p > 0.05$, *: $p < 0.05$, **: $p < 0.01$, ***: $p < 0.001$, ****: $p < 0.001$).

enhanced STING activation and improved immunotherapy, which may provide new insights into the clinical management of tumor immunotherapy.

Several recent studies have indicated that activation of STING pathway in tumors can inhibit tumor growth by activating the cross-presenting function of APC, followed by the infiltration of T cells in tumors and immunogenic tumor regression.[2,20,23,24] Recently, an interesting study found that Mn^{2+} activates innate immunity via the STING pathway in mouse model.[34] However, the administration of Mn^{2+} was found to result in systemic toxicity. Hence, accurate tumor targeting and sufficient Mn^{2+} accumulation at the tumor sites with low toxicity is needed. S. L. O'Neal and W. Zheng, 2015 found that after oral administration of 50 mg/kg Mn^{2+} per day for 10 weeks in rats, the half-life of Mn^{2+} reached 143 days on average in the bone and between 52 and 74 days in the brain. As a cofactor of various enzymes, changes in Mn^{2+} levels alter body metabolite levels. Intraperitoneal injections of 15 mg/kg Mn^{2+} per day can cause Parkinson's disease.[37] Humans are more likely to develop cardiovascular toxicity with exposure to Mn^{2+}.[38] Hence, the *in vivo* antitumor immunity effects of manganese-containing nanomaterials have been studied.[39–43] Therefore, in this study, we developed RGD peptide-targeted and Cy5.5-labeled RGD-$MnFe_2O_4$ nanoparticles. The FMI and MRI dual modality
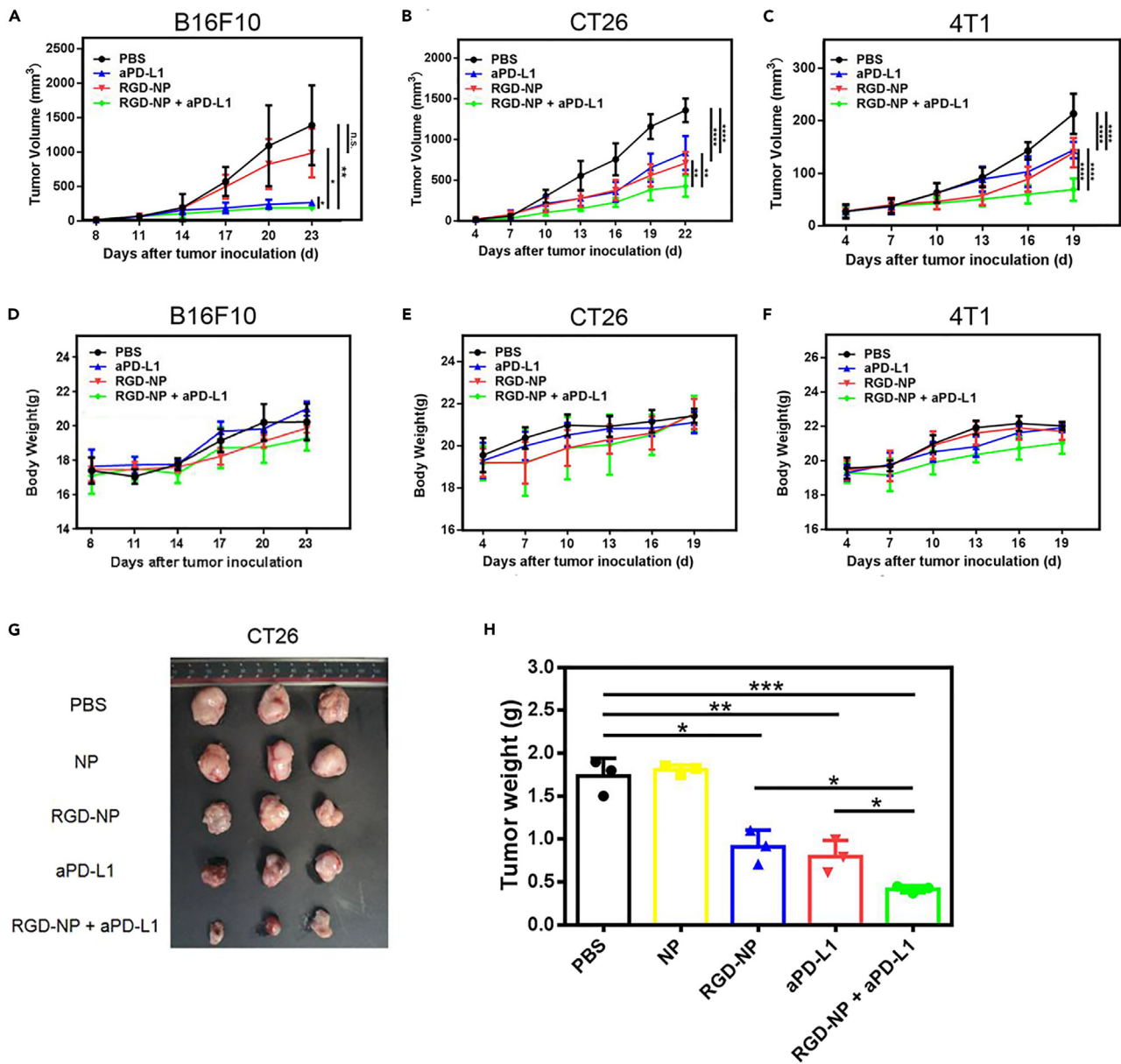
Figure 4. Antitumor effects of combined RGD-NP and aPD-L1 immunotherapy

(A–C) Tumor volume was monitored dynamically with different treatments on B16F10, CT26, and 4T1 tumors. (n = 6–10).

(D–F) The mouse body weight in each group was measured dynamically during the treatment period.

(G and H) Quantification of tumor weights and representative images of tumors at the end of CT26 treatment. Data are represented as mean ± SEM. (ns: p > 0.05, *: p < 0.05, **: p < 0.01, ***: p < 0.001, ****: p < 0.001).

imaging data showed that there was more RGD-NP accumulation with longer retention at tumor sites owing to the active targeting driving force of the RGD peptide. Moreover, the STING pathway was activated by RGD-NP in DCs both *in vitro* and *in vivo*. RGD-NP can also reduce the expression of immunosuppressive factors and induce the expression of antitumor cytokines such as IL-12 and IFN-β in the tumor, which illustrate the ability of RGD-NP to provide a relatively good immune-active environment.

aPD-L1 immunotherapy shows partial response to pembrolizumab for cancer patients.[8,49] One of the reasons for this is insufficient cross-presentation between APC and T cells. DCs are the most potent APCs. Tumor-derived factors like VEGF, M-CSF, and IL-1β can recruit myeloid suppressor cells, prevent the differentiation of precursor DCs into mature DCs, and further inhibit the infiltration of cytotoxic CD8+ T cells in tumors.[50] The STING pathway is usually silenced in tumors such as colorectal carcinoma and melanoma.[51,52] In our study, we found that our
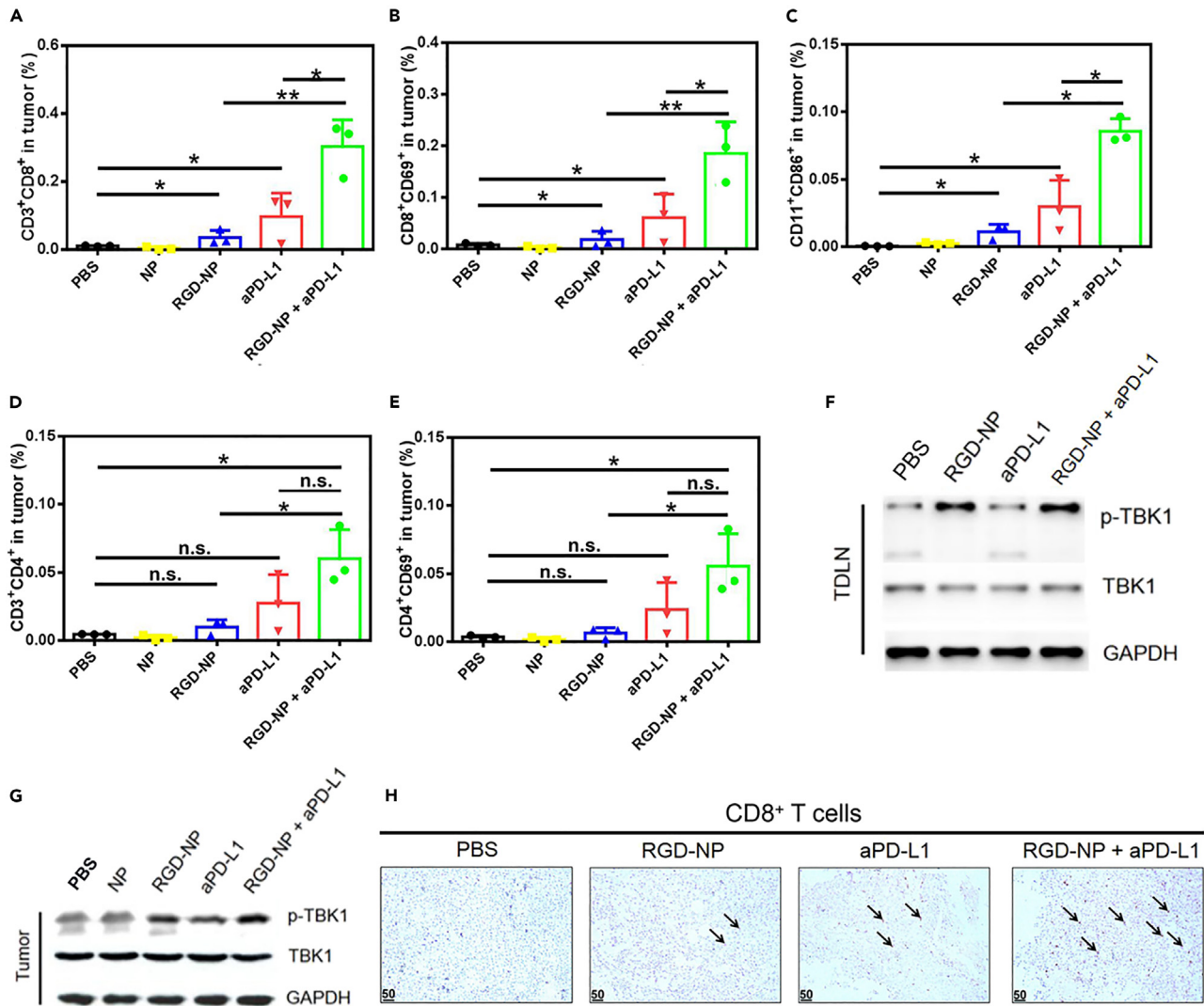
Figure 5. RGD-NP promote the recruitment of tumor-infiltrating cytotoxic T lymphocytes (CTLs)

(A–E) Flow cytometry results of tumors harvested to analyze tumor-infiltrating leukocytes with different treatments.

(F and G) Tumors and lymph nodes were lysed to obtain protein samples. Relative amounts of p-TBK1, total TBK1, and GAPDH were measured via western blot.

(H) Immunohistochemical staining of CD8$^+$ T cells in CT26 tumors. Scale bar, 50 μm Data are represented as mean $\pm$ SEM. (ns: $p > 0.05$, *: $p < 0.05$, **: $p < 0.01$, ***: $p < 0.001$, ****: $p < 0.001$).

developed RGD-NP can not only activate DCs but also can upregulate PD-L1 expression levels in tumors. Hence, we combined RGD-NP and aPD-L1 immunotherapy. The data showed that the combined immunotherapy could effectively increase the immunotherapeutic efficacy with effective inhibition of tumor growth, and the efficacy was validated in several tumor xenografts, such as 4T1, CT26, and B16F10 tumors. The underlying functional mechanism for combined immunotherapy is mainly through enhancing the infiltration level and activation status of CD8$^+$ and CD4$^+$ T cells and DCs. Finally, we monitored the toxicity of RGD-NP in combination with immunotherapy and found it is relatively safe with no obvious body weight loss or major organ toxicity.

In conclusion, our study developed a multifunctional Cy5.5-RGD-NP and provided a new method for the targeted imaging and improving tumor immunotherapy. Our developed Cy5.5-RGD-NP is multifunctional for FMI/MRI dual-modality imaging, and can be utilized for monitoring their *in vivo* biodistribution. Moreover, Cy5.5-RGD-NP can activate STING signaling pathway and up-regulating PD-L1 expression, which can synergize with aPD-L1 therapy to improve the antitumor therapeutic efficacy with no obvious toxicity. The underlying mechanism was further analyzed and the tumor infiltrating lymphocytes were responsible for the main antitumor immunotherapy. Moreover, it is reported that manganese-containing nanomaterials can decompose H_2O_2 to produce O_2 to mitigate tumor hypoxia, provide a relatively good immune microenvironment, and improve the immunotherapeutic effect.[35]

Limitations of the study

Fe_3O_4 nanoparticles and RGD peptides were approved by Food and Drug Administration (FDA) thanks to their unique properties in cancer diagnosis and cancer therapy with low toxicity but we have not carried out clinical trails. We verified that combining RGD-$MnFe_2O_4$ enhance the antitumor efficacy of aPD-L1 in several types of subcutaneous tumor model through STING pathway. But we cannot exclude the possibility that there are other mechanisms in this process.

STAR★METHODS

Detailed methods are provided in the online version of this paper and include the following:

- KEY RESOURCES TABLE
- RESOURCE AVAILABILITY
  - Lead contact
  - Materials availability
  - Data and code availability
- EXPERIMENTAL MODEL AND STUDY PARTICIPANT DETAILS
- METHOD DETAILS
  - Synthesis and characterization of RGD-NPs
  - Fluorescence molecular imaging (FMI) of the biodistribution of Cy5.5-$MnFe_2O_4$ (Cy5.5-NP) or Cy5.5-RGD-$MnFe_2O_4$ (Cy5.5-RGD-NP)
  - Tumor treatment experiment in subcutaneous tumor models
  - Bone marrow-derived dendritic cell (BMDC) isolation
  - Evaluation of STING pathway activation
  - Tumor-infiltrating lymphocyte (TIL) analysis
  - Cytotoxicity assays
  - Alanine transaminase (ALT) and aspartate transaminase (AST) analyses
  - Histology of major organs
- QUANTIFICATION AND STATISTICAL ANALYSIS

SUPPLEMENTAL INFORMATION

Supplemental information can be found online at https://doi.org/10.1016/j.isci.2024.109062.

AUTHOR CONTRIBUTIONS

S.G. conceptualization: equal; data curation: lead; formal analysis: lead; investigation: lead; methodology: equal; validation: lead; writing-original draft: equal; writing-review & editing: equal.

X.L. conceptualization: equal; data curation: equal; methodology: equal; project administration: equal; resources: equal; supervision: supporting; validation: supporting; writing-original draft: supporting; writing-review & editing: supporting.

Y.D. conceptualization: equal; data curation: supporting; formal analysis: equal; funding acquisition: lead; investigation: equal; methodology: equal; resources: lead; supervision: equal; writing-original draft: equal; writing-review & editing: equal.

J.T. conceptualization: supporting; funding acquisition: lead; methodology: equal; resources: lead; supervision: supporting.

DECLARATION OF INTERESTS

The authors declare no conflict of interest.

REFERENCES

1. Topalian, S.L., Drake, C.G., and Pardoll, D.M. (2015). Immune checkpoint blockade: a common denominator approach to cancer therapy. Cancer Cell 27, 450–461. https://doi.org/10.1016/j.ccell. 2015.03.001.

2. Zou, W., Wolchok, J.D., and Chen, L. (2016). PD-L1 (B7-H1) and PD-1 pathway blockade for cancer therapy: Mechanisms, response biomarkers, and combinations. Sci. Transl. Med. 8, 328rv4. https://doi.org/10.1126/scitranslmed.aad7118.

3. Liu, X., Pu, Y., Cron, K., Deng, L., Kline, J., Frazier, W.A., Xu, H., Peng, H., Fu, Y.X., and Xu, M.M. (2015). CD47 blockade triggers T cell-mediated destruction of immunogenic tumors. Nat. Med. 21, 1209–1215. https://doi.org/10.1038/nm.3931.

4. Du, Y., Qi, Y., Jin, Z., and Tian, J. (2019). Noninvasive Imaging in Cancer Immunotherapy: The Way to Precision Medicine. Cancer Lett. 466, 13–22. https://doi.org/10.1016/j.canlet.2019.08.009.

5. Du, Y., Jin, Y., Sun, W., Fang, J., Zheng, J., and Tian, J. (2019). Advances in molecular imaging of immune checkpoint targets in malignancies: current and future prospect. Eur. Radiol. 29, 4294–4302. https://doi.org/10.1007/s00330-018-5814-3.

6. Cheng, Z., Du, Y., Yu, L., Yuan, Z., and Tian, J. (2022). Effects of glycolysis on the polarization and function of tumor-associated macrophages. Mol. Imag. Biol. 24, 264–279. https://doi.org/10.3892/ijo.2023.5518.

7. Wang, H., Hu, S., Chen, X., Shi, H., Chen, C., Sun, L., and Chen, Z.J. (2017). cGAS is essential for the antitumor effect of immune checkpoint blockade. Proc. Natl. Acad. Sci. USA 114, 1637–1642. https://doi.org/10.1073/pnas.1621363114.

8. Le, D.T., Uram, J.N., Wang, H., Bartlett, B.R., Kemberling, H., Eyring, A.D., Skora, A.D., Luber, B.S., Azad, N.S., Laheru, D., et al. (2015). PD-1 blockade in tumors with mismatch-repair deficiency. N. Engl. J. Med. 372, 2509–2520. https://doi.org/10.1056/NEJMoa1500596.

9. Formenti, S.C., Rudqvist, N.P., Golden, E., Cooper, B., Wennerberg, E., Lhuillier, C., Vanpouille-Box, C., Friedman, K., Ferrari de Andrade, L., Wucherpfennig, K.W., et al. (2018). Radiotherapy induces responses of lung cancer to CTLA-4 blockade. Nat. Med. 24, 1845–1851. https://doi.org/10.3892/ijo.2023.5518.

10. Hegde, P.S., and Chen, D.S. (2020). Top 10 challenges in cancer immunotherapy. Immunity 52, 17–35. https://doi.org/10.1016/j.immuni.2019.12.011.

11. Salman, S., Meyers, D.J., Wicks, E.E., Lee, S.N., Datan, E., Thomas, A.M., Anders, N.M., Hwang, Y., Lyu, Y., Yang, Y., et al. (2022). HIF inhibitor 32-134D eradicates murine hepatocellular carcinoma in combination with anti-PD1 therapy. J. Clin. Invest. 132, 2. https://doi.org/10.3892/ijo.2023.5518.

12. Wculek, S.K., Cueto, F.J., Mujal, A.M., Melero, I., Krummel, M.F., and Sancho, D. (2020). Dendritic cells in cancer immunology and immunotherapy. Nat. Rev. Immunol. 20, 7–24. https://doi.org/10.3892/ijo.2023.5518.

13. Woo, S.R., Fuertes, M.B., Corrales, L., Spranger, S., Furdyna, M.J., Leung, M.Y.K., Duggan, R., Wang, Y., Barber, G.N., Fitzgerald, K.A., et al. (2014). STING-dependent cytosolic DNA sensing mediates innate immune recognition of immunogenic tumors. Immunity 41, 830–842. https://doi.org/10.1016/j.immuni.2014.10.017.

14. Fu, J., Kanne, D.B., Leong, M., Glickman, L.H., McWhirter, S.M., Lemmens, E., Mechette, K., Leong, J.J., Lauer, P., Liu, W., et al. (2015). STING agonist formulated cancer vaccines can cure established tumors resistant to PD-1 blockade. Sci. Transl. Med. 7, 283ra52. https://doi.org/10.1126/scitranslmed.aaa4306.

15. An, X., Zhu, Y., Zheng, T., Wang, G., Zhang, M., Li, J., Ji, H., Li, S., Yang, S., Xu, D., et al. (2019). An Analysis of the Expression and Association with Immune Cell Infiltration of the cGAS/STING Pathway in Pan-Cancer. Mol. Ther. Nucleic Acids 14, 80–89. https://doi.org/10.1016/j.omtn.2018.11.003.

16. Li, S., Luo, M., Wang, Z., Feng, Q., Wilhelm, J., Wang, X., Li, W., Wang, J., Cholka, A., Fu, Y.x., et al. (2021). Prolonged activation of innate immune pathways by a polyvalent STING agonist. Nat. Biomed. Eng. 5, 455–466. https://doi.org/10.3892/ijo.2023.5518.

17. Yi, M., Niu, M., Zhang, J., Li, S., Zhu, S., Yan, Y., Li, N., Zhou, P., Chu, Q., and Wu, K. (2021). Combine and conquer: manganese synergizing anti-TGF-β/PD-L1 bispecific antibody YM101 to overcome immunotherapy resistance in non-inflamed cancers. J. Hematol. Oncol. 14, 1. https://doi.org/10.1186/s13045-021-01155-6.

18. Ishikawa, H., and Barber, G.N. (2008). STING is an endoplasmic reticulum adaptor that facilitates innate immune signalling. Nature 455, 674–678. https://doi.org/10.1038/nature07317.

19. Wu, J., Sun, L., Chen, X., Du, F., Shi, H., Chen, C., and Chen, Z.J. (2013). Cyclic GMP-AMP is an endogenous second messenger in innate immune signaling by cytosolic DNA. Science 339, 826–830. https://doi.org/10.1126/science.1229963.

20. Chen, H., Sun, H., You, F., Sun, W., Zhou, X., Chen, L., Yang, J., Wang, Y., Tang, H., Guan, Y., et al. (2011). Activation of STAT6 by STING is critical for antiviral innate immunity. Cell 147, 436–446. https://doi.org/10.1016/j.cell.2011.09.022.

21. Ablasser, A., and Chen, Z.J. (2019). cGAS in action: Expanding roles in immunity and inflammation. Science 363, eaat8657. https://doi.org/10.1126/science.aat8657.

22. Mullard, A. (2018). Can innate immune system targets turn up the heat on 'cold' tumours? Nat. Rev. Drug Discov. 17, 3–5. https://doi.org/10.1038/nrd.2017.264.

23. Ergun, S.L., Fernandez, D., Weiss, T.M., and Li, L. (2019). STING polymer structure reveals mechanisms for activation, hyperactivation, and inhibition. Cell 178, 290–301.e10. https://doi.org/10.1016/j.cell.2019.05.036.

24. Shae, D., Becker, K.W., Christov, P., Yun, D.S., Lytton-Jean, A.K.R., Sevimli, S., Ascano, M., Kelley, M., Johnson, D.B., Balko, J.M., et al. (2019). Endosomolytic polymersomes increase the activity of cyclic dinucleotide STING agonists to enhance cancer immunotherapy. Nat. Nanotechnol. 14, 269–278. https://doi.org/10.1038/s41565-018-0342-5.

25. Corrales, L., Glickman, L.H., McWhirter, S.M., Kanne, D.B., Sivick, K.E., Katibah, G.E., Woo, S.R., Lemmens, E., Banda, T., Leong, J.J., et al. (2015). Direct activation of STING in the tumor microenvironment leads to potent and systemic tumor regression and immunity. Cell Rep. 11, 1018–1030. https://doi.org/10.1016/j.celrep.2015.04.031.

26. Ohkuri, T., Kosaka, A., Ishibashi, K., Kumai, T., Hirata, Y., Ohara, K., Nagato, T., Oikawa, K., Aoki, N., Harabuchi, Y., et al. (2017). Intratumoral administration of cGAMP transiently accumulates potent macrophages for anti-tumor immunity at a mouse tumor site. Cancer Immunol. Immunother. 66, 705–716. https://doi.org/10.1007/s00262-017-1975-1.

27. Li, T., Cheng, H., Yuan, H., Xu, Q., Shu, C., Zhang, Y., Xu, P., Tan, J., Rui, Y., Li, P., and Tan, X. (2016). Antitumor activity of cGAMP via stimulation of cGAS-cGAMP-STING-IRF3 mediated innate immune response. Sci. Rep. 6, 19049. https://doi.org/10.1038/srep19049.

28. Kosaka, A., Ishibashi, K., Nagato, T., Kitamura, H., Fujiwara, Y., Yasuda, S., Nagata, M., Harabuchi, S., Hayashi, R., Yajima, Y., et al. (2021). CD47 blockade enhances the efficacy of intratumoral STING-targeting therapy by activating phagocytes. J. Exp. Med. 218, e20200792. https://doi.org/10.1084/jem.20200792.

29. Liu, Y., Crowe, W.N., Wang, L., Lu, Y., Petty, W.J., Habib, A.A., and Zhao, D. (2019). An inhalable nanoparticulate STING agonist synergizes with radiotherapy to confer long-term control of lung metastases. Nat. Commun. 10, 5108. https://doi.org/10.1038/s41467-019-13094-5.

30. Li, S., Luo, M., Wang, Z., Feng, Q., Wilhelm, J., Wang, X., Li, W., Wang, J., Cholka, A., Fu, Y.X., et al. (2021). Prolonged activation of innate immune pathways by a polyvalent STING agonist. Nat. Biomed. Eng. 5, 455–466. https://doi.org/10.1038/s41551-020-00675-9.

31. Ramanjulu, J.M., Pesiridis, G.S., Yang, J., Concha, N., Singhaus, R., Zhang, S.Y., Tran, J.L., Moore, P., Lehmann, S., Eberl, H.C., et al. (2018). Design of amidobenzimidazole STING receptor agonists with systemic activity. Nature 564, 439–443. https://doi.org/10.1038/s41586-018-0705-y.

32. Ding, B., Shao, S., Jiang, F., Dang, P., Sun, C., Huang, S., Ma, P., Jin, D., Kheraif, A.A.A., and Lin, J. (2019). MnO2-disguised upconversion hybrid nanocomposite: an ideal architecture for tumor microenvironment-triggered UCL/MR bioimaging and enhanced chemodynamic therapy. Nanoscale 31, 2651–2660. https://doi.org/10.1021/acs.chemmater.9b00893.

33. Zhu, C., Ma, Q., Gong, L., Di, S., Gong, J., Wang, Y., Xiao, S., Zhang, L., Zhang, Q., Fu, J.J., et al. (2022). Manganese-based multifunctional nanoplatform for dual-modal imaging and synergistic therapy of breast cancer. Acta Biomater. 141, 429–439. https://doi.org/10.1016/j.actbio.2022.01.019.

34. Wang, C., Guan, Y., Lv, M., Zhang, R., Guo, Z., Wei, X., Du, X., Yang, J., Li, T., Wan, Y., et al. (2018). Manganese increases the sensitivity of the cGAS-STING pathway for double-stranded DNA and is required for the host defense against DNA viruses. Immunity 48, 675–687.e7. https://doi.org/10.1016/j.immuni.2018.03.017.

35. Hu, D., Chen, L., Qu, Y., Peng, J., Chu, B., Shi, K., Hao, Y., Zhong, L., Wang, M., and Qian, Z. (2018). Oxygen-generating hybrid polymeric nanoparticles with encapsulated doxorubicin and chlorin e6 for trimodal imaging-guided combined chemo-photodynamic therapy.

Theranostics *8*, 1558–1574. https://doi.org/10.7150/thno.22989.

36. Wang, Z., Xue, X., Lu, H., He, Y., Lu, Z., Chen, Z., Yuan, Y., Tang, N., Dreyer, C.A., Quigley, L., et al. (2020). Two-way magnetic resonance tuning and enhanced subtraction imaging for non-invasive and quantitative biological imaging. Nat. Nanotechnol. *15*, 482–490. https://doi.org/10.1038/s41565-020-0678-5.

37. O'Neal, S.L., and Zheng, W. (2015). Manganese toxicity upon overexposure: a decade in review. Curr. Environ. Health Rep. *2*, 315–328. https://doi.org/10.1007/s40572-015-0056-x.

38. Jiang, Y., and Zheng, W. (2005). Cardiovascular toxicities upon manganese exposure. Cardiovasc. Toxicol. *5*, 345–354. https://doi.org/10.1385/ct:5:4:345.

39. Hou, L., Tian, C., Yan, Y., Zhang, L., Zhang, H., and Zhang, Z. (2020). Manganese-based nanoactivator optimizes cancer immunotherapy via enhancing innate immunity. ACS Nano *14*, 3927–3940. https://doi.org/10.1021/acsnano.9b06111.

40. Song, Y., Liu, Y., Teo, H.Y., Hanafi, Z.B., Mei, Y., Zhu, Y., Chua, Y.L., Lv, M., Jiang, Z., and Liu, H. (2021). Manganese enhances the antitumor function of CD8+ T cells by inducing type I interferon production. Cell. Mol. Immunol. *18*, 1571–1574. https://doi.org/10.1038/s41423-020-00524-4.

41. Wang, C., Sun, Z., Zhao, C., Zhang, Z., Wang, H., Liu, Y., Guo, Y., Zhang, B., Gu, L., Yu, Y., et al. (2021). Maintaining manganese in tumor to activate cGAS-STING pathway evokes a robust abscopal anti-tumor effect. J. Contr. Release *331*, 480–490. https://doi.org/10.1016/j.jconrel.2021.01.036.

42. Tian, H., Wang, G., Sang, W., Xie, L., Zhang, Z., Li, W., Yan, J., Tian, Y., Li, J., Li, B., and Dai, Y. (2022). Manganese-phenolic nanoadjuvant combines sonodynamic therapy with cGAS-STING activation for enhanced cancer immunotherapy. Nano Today *43*, 101405. https://doi.org/10.1016/j.nantod.2022.101405.

43. Zhang, R., Wang, C., Guan, Y., Wei, X., Sha, M., Yi, M., Jing, M., Lv, M., Guo, W., Xu, J., et al. (2021). Manganese salts function as potent adjuvants. Cell. Mol. Immunol. *18*, 1222–1234. https://doi.org/10.1038/s41423-021-00669-w.

44. Avraamides, C.J., Garmy-Susini, B., and Varner, J.A. (2008). Integrins in angiogenesis and lymphangiogenesis. Nat. Rev. Cancer *8*, 604–617. https://doi.org/10.1038/nrc2353.

45. Xie, J., Chen, K., Lee, H.Y., Xu, C., Hsu, A.R., Peng, S., Chen, X., and Sun, S. (2008). Ultrasmall c(RGDyK)-coated Fe3O4 nanoparticles and their specific targeting to integrin alpha(v)beta3-rich tumor cells. J. Am. Chem. Soc. *130*, 7542–7543. https://doi.org/10.1021/ja802003h.

46. Li, R., Zhou, Y., Liu, Y., Jiang, X., Zeng, W., Gong, Z., Zheng, G., Sun, D., and Dai, Z. (2022). Asymmetric, amphiphilic RGD conjugated phthalocyanine for targeted photodynamic therapy of triple negative breast cancer. Signal Transduct. Targeted Ther. *7*, 64. https://doi.org/10.1038/s41392-022-00906-2.

47. Dumont, R.A., Deininger, F., Haubner, R., Maecke, H.R., Weber, W.A., and Fani, M. (2011). Novel (64)Cu- and (68)Ga-labeled RGD conjugates show improved PET imaging of α(v)β(3) integrin expression and facile radiosynthesis. J. Nucl. Med. *52*, 1276–1284. https://doi.org/10.2967/jnumed.111.087700.

48. Waldman, A.D., Fritz, J.M., Lenardo, M.J., and Lenardo, M.J. (2020). A guide to cancer immunotherapy: from T cell basic science to clinical practice. Nat. Rev. Immunol. *20*, 651–668. https://doi.org/10.1038/s41577-020-0306-5.

49. Hamid, O., Robert, C., Daud, A., Hodi, F.S., Hwu, W.J., Kefford, R., Wolchok, J.D., Hersey, P., Joseph, R.W., Weber, J.S., et al. (2013). Safety and tumor responses with lambrolizumab (anti-PD-1) in melanoma. N. Engl. J. Med. *369*, 134–144. https://doi.org/10.1056/NEJMoa1305133.

50. Pinzon-Charry, A., Maxwell, T., and López, J.A. (2005). Dendritic cell dysfunction in cancer: a mechanism for immunosuppression. Immunol. Cell Biol. *83*, 451–461. https://doi.org/10.1111/j.1440-1711.2005.01371.x.

51. Xia, T., Konno, H., and Barber, G.N. (2016). Recurrent loss of STING signaling in melanoma correlates with susceptibility to viral oncolysis. Can. Res. *76*, 6747–6759. https://doi.org/10.1158/0008-5472.CAN-16-1404.

52. Xia, T., Konno, H., Ahn 1, J., and Barber, G.N. (2016). Deregulation of STING signaling in colorectal carcinoma constrains DNA damage responses and correlates with tumorigenesis. Cell Rep. *14*, 282. https://doi.org/10.1016/j.celrep.2015.12.029.

53. Schindelin, J., Arganda-Carreras, I., Frise, E., Kaynig, V., Longair, M., Pietzsch, T., Preibisch, S., Rueden, C., Saalfeld, S., Schmid, B., et al. (2012). Fiji: an open-source platform for biological-image analysis. Nat. Methods *9*, 676–682. https://doi.org/10.1038/nmeth.2019.

iScience Article

STAR★METHODS

KEY RESOURCES TABLE

REAGENT or RESOURCE	SOURCE	IDENTIFIER
Antibodies		
GAPDH (D16H11) XP® Rabbit mAb	CST	RRID: AB_10622025
TBK1/NAK (E8I3G) Rabbit mAb	CST	RRID: AB_2827657
Phospho-TBK1/NAK (Ser172) (D52C2) XP® Rabbit mAb	CST	RRID: AB_10693472
HRP-conjugated Affinipure Goat Anti-Mouse IgG(H+L)	Proteintech	RRID: AB_2722565
HRP-conjugated Affinipure Goat Anti-Rabbit IgG(H+L)	Proteintech	RRID: AB_2722564
TMEM173/STING Polyclonal antibody	Proteintech	RRID: AB_10665370
Alexa Fluor647-conjugated goat anti-rabbit antibody	CST	RRID: AB_10693544
PD-L1/CD274 (C-terminal) Polyclonal antibody	Proteintech	RRID: AB_2881052
BD Pharmingen™ PerCP-Cy™5.5 Rat Anti-Mouse CD45	BD	RRID: AB_394003
FITC anti-mouse CD3 Antibody	BioLegend	RRID: AB_312660
PE/Cyanine7 anti-mouse CD8b.2 Antibody	BioLegend	RRID: AB_2564384
APC anti-mouse CD4	BioLegend	RRID: AB_312696
PE anti-mouse CD69	BioLegend	RRID: AB_2936560
BV510 anti-mouse CD11c	BioLegend	RRID: AB_2562010
APC anti-mouse CD86	BioLegend	RRID: AB_493342
Chemicals, peptides, and recombinant proteins		
Oleic acid	Sigma-aldrich	Cat# O1008
Oleyl alcohol	Sigma-aldrich	Cat# 369314
Dihydroxyhydrocinnamic acid	Sigma-aldrich	Cat# 102601
Tetrahydrofuran	Sigma-aldrich	Cat# 186562
N-(3-dimethylaminopropyl)-ethylcarbodiimide hydrochloride	Sigma-aldrich	Cat# 03449
NHS	Sigma-aldrich	Cat# 130672
Dialysis membranes	Sangon Biotech	Cat# 39391
Cy5.5-NH2	Xi'an Ruixi	Cat# R-H-0013
red blood cell lysis buffer	Solarbio	Cat# R1010
GM-CSF	PeproTech	Cat# 315-03
IL-4	PeproTech	Cat# 214-14
SDS	Sangon Biotech	Cat# A600485
DTT	Sangon Biotech	Cat# A620058
Bromophenol blue	Sangon Biotech	Cat# A602230
Tris	Sangon Biotech	Cat# A600194
Phosphatase inhibitors	ThermoFisher	Cat# A32959
Gly	Sangon Biotech	Cat# A610236
TBST	Applygen	Cat# B1009
Mounting medium	Solarbio	Cat# S2110
c(RGDyK)	Sangon Biotech	N/A

(Continued on next page)

Continued

REAGENT or RESOURCE	SOURCE	IDENTIFIER
Experimental models: Cell lines		
Mouse 4T1 cells	ATCC	Cat# CRL-2539
Mouse CT26 cells	ATCC	Cat# CRL-2638
Mouse B16F10 cells	ATCC	Cat# CRL-6475
DC2.4	BLUEFBIO Corporation	Cat# BFN60804347
BMDC	This paper	N/A
CT26-GFP	Hangzhou Meiseng Technical Corporation in China	N/A
Experimental models: Organisms/strains		
Mouse: C57BL/6	Vital River Laboratory Animal Technology Corporation	Cat# 211
Mouse: BALB/c	Vital River Laboratory Animal Technology Corporation	Cat# 213
Oligonucleotides		
Primer: Arg forward:AATGAAGAGCTGGCTGGTGT	Sangon Biotech	N/A
Primer: Arg reverse:CTGGTTGTCAGGGGAGTGTT	Sangon Biotech	N/A
Primer: β-actin forward:GGCTGTATTCCCCTCCATCG	Sangon Biotech	N/A
Primer: β-actin reverse:CCAGTTGGTAACAATGCCATGT	Sangon Biotech	N/A
Primer: IFNb1 forward:GGGTGGAATGAGACTATTGTTGTACGTCT	Sangon Biotech	N/A
Primer: IFNb1 reverse:GTGGAGAGCAGTTGAGGACATCTC	Sangon Biotech	N/A
Primer: IL12 forward:CCATCACTGTCAAAGAGTTTCTAGATGCTG	Sangon Biotech	N/A
Primer: IL12 reverse:CAAATTCCATTTTCCTTCTTGTGGAGCAGC	Sangon Biotech	N/A
Primer: IL10 forward:GTGGAGCAGGTGAAGAGTGA	Sangon Biotech	N/A
Primer: IL10 reverse:TCGGAGAGAGGTACAAACGAG	Sangon Biotech	N/A
Software and algorithms		
FlowJo v.9.9.4	FlowJo, LLC	https://www.www.flowjo.com
Fiji	Schindelin et al.[53]	https://fiji.sc
Living Image Software (IVIS Imaging Systems)	PerkinElmer	https://www.perkinelmer.com.cn/
Case Viewer	3DHistech	https://www.3dhistech.com/solutions/caseviewer/
Graphprism 6.0	Graphpad	https://www.graphpad.com/resources

RESOURCE AVAILABILITY

Lead contact

Further information and requests for resources and reagents should be directed to and will be fulfilled by the lead contact, Jie Tian, jie.tian@ia. ac.cn (lead contact).

Materials availability

All unique/stable reagents generated in this study are available from the lead contact with a completed Materials Transfer Agreement.

Data and code availability

- Research data are not shared.
- This paper does not report original code.
- Any additional information required to reanalyse the data reported in this paper is available from the lead contact upon request.

EXPERIMENTAL MODEL AND STUDY PARTICIPANT DETAILS

Mouse breast 4T1 tumor cells, colon carcinoma CT26 cells, and melanoma B16F10 cells were obtained from the American Type Culture Collection (ATCC, USA). CT26-GFP tumor cells were obtained form Hangzhou Meiseng Technical Corporation in China. The cells were cultured in RPMI1640 medium (Macgene, CM10040) with 10% fetal bovine serum (FBS) (Gibco, 10099141C) and 1% penicillin-streptomycin (Macgene, CC004) in a 5% CO_2 incubator at 37°C. 1×10^6 tumor cells were suspended in 0.1 mL of phosphate-buffered saline (PBS) and injected subcutaneously into the right hind back of C57BL/6 or BALB/c mice (17-20 g, 4-5 weeks, male, Vital River Laboratory Animal Technology Corporation). All animal experiments were performed in accordance with the guidelines of the Institutional Animal Care and Use Committee (Permit No: IA21-2203-24) of the Institute of Automation, Chinese Academy of Sciences.

METHOD DETAILS

Synthesis and characterization of RGD-NPs

The $MnFe_2O_4$ nanoparticles were synthesized as shown in Figure 1A via the dynamic simultaneous thermal decomposition of iron-eruciate and manganese-oleate precursors in the presence of oleic acid, oleyl alcohol, and benzyl ether. First, 1.0 g of iron-eruciate precursor, 0.5 g of manganese-oleate precursor, 2 mmol of oleic acid, and 6 mmol of oleyl alcohol were dispersed in 10 g of benzyl ether at 20°C. After, the mixture was heated to 265°C at a rate of 5°C/min and kept at 265°C for 30 min under a stable argon flow. The mixture was rapidly cooled to 20°C, and 20 mL of ethanol was added to the solution. The precipitated nanoparticles were separated via centrifugation. Surface modification of the $MnFe_2O_4$ nanoparticles (NP) with 3,4- dihydroxyhydrocinnamic acid (DHCA) was performed using a ligand-exchange reaction. For carboxyl functionalization, 20 mg of NP and 50 mg of DHCA were dispersed in 5 mL of tetrahydrofuran, and the mixed system was heated to 50°C under magnetic stirring for 3 h. Subsequently, the mixture was cooled to room temperature, 0.5 mL of NaOH (0.5 M) was added, and the supernatant was removed via centrifugation and then the precipitates were dispersed in deionized water for further use. Then, c(RGDyK) (Shang Hai Sangon BIotech Corporation, China) was anchored to the nanoparticles through a dehydration reaction between the carboxylic acid and the amine. The nanoparticles were mixed with 10 mol N-(3-dimethylaminopropyl) -ethylcarbodiimide hydrochloride (EDC-HCl) and NHS at room temperature for 24 h, and free EDC and NHS were removed using dialysis membranes (5000 Da), followed by adding c(RGDyk) and the reaction was continued for another 2 h. Cy5.5 fluorescent dye (Xi'an Ruixi Biological Technology Corporation) was conjugated to the RGD-NP. Shape and morphology of RGD-NP were obtained by transmission electron microscopy (Tecnia G2 F20 S-Twin, FEI). The zeta potential and hydrodynamic diameter of RGD-NP were determined by Malvern Zetasizer nano-ZS dynamic light scatting (DLS, Zetasizer Nano ZS90, Malvern Instruments, UK) instrument.

Fluorescence molecular imaging (FMI) of the biodistribution of Cy5.5-MnFe₂O₄ (Cy5.5-NP) or Cy5.5-RGD-MnFe₂O₄ (Cy5.5-RGD-NP)

The dynamic biodistribution of Cy5.5-NP or Cy5.5-RGD-NP was observed using non-invasive *in vivo* FMI with IVIS (*In vivo* imaging system). Six mice were divided into two groups, and FMI data were obtained from 0 to 48 h after tail vein injection of Cy5.5-RGD-NP at the indicated time points (Ex = 683 nm, Em = 703 nm) with Cy5.5-NP as control. The mice were sacrificed via cervical dislocation at 48 h after intravenous injection of nanoparticles, and major organs, including the tumor, liver, heart, spleen, kidney, and brain, were further imaged *ex vivo*. The signal-to-background ratio (SBR) was calculated with following formula: SBR = Fluorescence light intensity$_{tumor}$/Fluorescence light intensity$_{background}$. CT26 subcutaneous tumor model was further used for MRI. After intravenous injection of 0.1 mL of 1 mg/mL RGD-NP or $MnFe_2O_4$, the mice were imaged using a 7T MRI scanner (Bruker BioSpec 70/20 USR, Billerica, MA, USA) at indicated time points.

Tumor treatment experiment in subcutaneous tumor models

To evaluate the ability of RGD-$MnFe_2O_4$ to enhance the antitumor efficacy in aPD-L1 treatment, we established subcutaneous tumor models (1×10^6 tumor cells for the 4T1, CT26, and B16F10 models). Nanoparticles and aPD-L1 were administered when the tumor volume reached 50 mm^3. 0.1 mg RGD-$MnFe_2O_4$ in 0.1 mL of PBS was injected intravenously, and 0.2 mg of aPD-L1 in 0.2 mL PBS was injected intraperitoneally

alone or 12 h after RGD-MnFe$_2$O$_4$ injection. These treatments were given once every 3 days. The tumor volume was calculated using formula: $V = length \times width^2/2$.

Bone marrow-derived dendritic cell (BMDC) isolation

We obtained BMDCs from the bone marrow of 8–10-week-old C57BL/6 mice. Briefly, the mice were sacrificed by cervical dislocation and immersed in 75% alcohol. The tibia and femur were rinsed with RPMI1640 medium without FBS. After removing the red blood cells with red blood cell lysis buffer (Solarbio, R1010), bone marrow cells were placed in a 24-well plate at a density of 5×10^5 cells per well. We prepared culture medium for inducing immature BMDCs, which contained 20 ng/mL of recombinant murine GM-CSF (PeproTech, 315-03) and 10 ng/mL of recombinant murine IL-4 (PeproTech, 214-14). Half of the culture medium was removed on days 2, 4, and 6, followed by adding equal volume of fresh medium, and immature BMDCs were obtained on day 7.

Evaluation of STING pathway activation

STING pathway activation was detected via western blotting and immunofluorescence. To obtain protein samples, cells were collected and lysed in 1x sodium dodecyl sulfate (SDS) lysis buffer (3% SDS, 0.03% bromophenol blue, 0.1 M DTT, 50 mM Tris-HCl pH = 6.8, and 1% phosphatase inhibitors) at 99°C for 10 min. Protein samples were resolved using 12% SDS-polyacrylamide gel electrophoresis. The proteins were transferred to polyvinylidene difluoride membranes (Solarbio, Millipore, HATF00010), which were rinsed in 1x TBST (Applygen, B1009) with 5% skimmed milk. After incubation with antibodies against GAPDH (1:1000 dilution; CST, 60004-1-Ig), TBK1 (1:1000 dilution; CST, 38066), and p-TBK1 (1:1000 dilution; CST, 5483) for 4 h at RT, the membrane was rinsed three times with TBST and incubated with horseradish peroxidase (HRP)-conjugated goat anti-mouse secondary antibodies (1:4000 dilution; Proteintech, SA00001-1) or goat anti-rabbit IgG (H+L) (1:4000 dilution; Proteintech, SA00001-2) for 30 min at RT.

In addition, we performed immunofluorescence to determine whether the STING protein accumulated around the nucleus after activation. Cells were seeded on coverslips and treated with nanoparticles. The samples were fixed and permeated with cold methanol for 15 min and rinsed three times with PBS. After blocking with 5% goat serum, the coverslips were incubated with STING antibody (1:500 dilution; Proteintech, 19851-1-AP) for 4 h at RT. The coverslips were washed three times with PBS, and Alexa Fluor647-conjugated goat anti-rabbit antibody was applied to the coverslips for 1 h in a moist, dark environment. Finally, the coverslips were covered on microscope slides with antifade Mounting medium (Solarbio, S2110) and examined under a fluorescence microscopy.

Tumor-infiltrating lymphocyte (TIL) analysis

The percentage of TILs was analyzed via fluorescence-activated cell sorting (FACS) using a BD Canto II flow cytometer (BD Biosciences). Tumor samples from all groups were harvested if there was a mouse with a tumor size of 1500 mm^3. The tumors were collected in 1640 medium with 1% FBS and minced. Followed by enzymolysis reaction with 0.25 mg/mL of collagenase IV (Merck, C4-28) and 50 ug/mL of ghDNaseI (Merck, 260913) at 37°C for 30 min and filtration through a 100-μm strainer. Then red blood cells were lysed with RBC lysis buffer (Solarbio, R1010). The cells were washed and incubated with fluorescence-labelled antibodies for 30 min, and then washed with PBS and analyzed via flow cytometer. The gates and quadrants were set based on the isotype control. TILs were defined as CD45$^+$ cells and were normalized to the total number of analyzed cells. CD8$^+$ T cells were defined as CD45$^+$ CD3$^+$ CD8$^+$ TILs. CD4$^+$ T cells were defined as CD45$^+$ CD3$^+$ CD4$^+$ TILs. Activated CD8$^+$ and CD4$^+$ T cells were defined as CD8$^+$ CD69$^+$ and CD4$^+$ CD69$^+$ cells, respectively. The activated DCs were defined as CD45$^+$ CD11$^+$ CD86$^+$ cells.

Cytotoxicity assays

In vitro cytotoxicity assays were performed using the CCK8 assay. 4T1, B16F10, and CT26 cells were seeded in 96-well plates and incubated overnight with different doses of nanoparticles. Then, the original medium was discarded and replaced with a culture medium containing 0.1, 0.5, 1, 2, 5, 10, 20, or 40 μg/mL of RGD-NP, and the cells were incubated for 24 or 48 h. Subsequently, cytotoxicity was evaluated using Cell Counting Kit-8 assay (Solarbio, CA1210) according to the manufacturer's instructions.

Alanine transaminase (ALT) and aspartate transaminase (AST) analyses

The toxicity of RGD-NP *in vivo* was evaluated by measuring ALT and AST levels. Blood was sampled from the orbital sinus and allowed to stand for 2 h at 4°C. The blood samples were then centrifuged at 3500 rpm at 4°C for 15 min, and the supernatant was collected to obtain serum samples. Finally, the serum samples were analyzed using an automatic biochemical analyzer (Hitachi, SOP7600P).

Histology of major organs

Organs were fixed overnight in 4% of paraformaldehyde. The samples were removed and dehydrated using a gradient of ethanol and xylene. After embedding the samples in paraffin overnight, paraffin sections were prepared using a rotary microtome. The sections were kept at 65°C for 15 min, followed by a rinse in xylene for 10 min, this step was repeated in fresh xylene, and the sections were rehydrated using gradient ethanol. The sections were rinsed with hematoxylin (Solarbio, G1120) for 10 s, destained in acidic ethanol, and rinsed in tap water. The sections were stained with eosin (Solarbio, G1120) for 30 s and transferred to distilled water. The dehydration step was repeated, and the sections were mounted with sufficient neutral balsam and examined with a slice scanning machine.

QUANTIFICATION AND STATISTICAL ANALYSIS

Statistical analysis was performed with GraphPad Prism (version 6.0, San Diego, CA). T-test was used for analyzing differences between groups. The mean values±SEM was showed in figure, and statistically signifcant differences marked with * indicate $P<0.05$, ** indicate $P<0.01$, *** indicate $P<0.001$ and **** indicate $P<0.0001$.